

# Collective dynamics of colloids at fluid interfaces

J. Bleibel<sup>1,2</sup>, A. Domínguez<sup>3</sup>, M. Oettel<sup>2</sup>, S. Dietrich<sup>1,4</sup>

<sup>1</sup> Max-Planck-Institut für Intelligente Systeme, Heisenbergstr. 3, 70569 Stuttgart, Germany

<sup>2</sup> Institut für Physik, WA 331, Johannes Gutenberg Universität Mainz, 55099 Mainz, Germany

<sup>3</sup> Física Teórica, Universidad de Sevilla, Apdo. 1065, 41080 Sevilla, Spain

<sup>4</sup> Institut für Theoretische und Angewandte Physik, Universität Stuttgart, Pfaffenwaldring 57, 70569 Stuttgart, Germany

November 8, 2018

**Abstract.** The evolution of an initially prepared distribution of micron sized colloidal particles, trapped at a fluid interface and under the action of their mutual capillary attraction, is analyzed by using Brownian dynamics simulations. At a separation  $\lambda$  given by the capillary length of typically 1 mm, the distance dependence of this attraction exhibits a crossover from a logarithmic decay, formally analogous to two-dimensional gravity, to an exponential decay. We discuss in detail the adaption of a particle–mesh algorithm, as used in cosmological simulations to study structure formation due to gravitational collapse, to the present colloidal problem. These simulations confirm the predictions, as far as available, of a mean–field theory developed previously for this problem. The evolution is monitored by quantitative characteristics which are particularly sensitive to the formation of highly inhomogeneous structures. Upon increasing  $\lambda$  the dynamics show a smooth transition from the spinodal decomposition expected for a simple fluid with short–ranged attraction to the self–gravitational collapse scenario.

**PACS.** 82.70.Dd – 47.11.Mn – 05.40.Jc

## 1 Introduction

The investigation of systems in low dimensions offers a rich spectrum of phenomena which are rather distinct from three–dimensional (3D) bulk properties. This is the case because structural properties of condensed matter depend sensitively on the spatial dimension. For example, in two–dimensional (2D) systems the solid–liquid phase transition is replaced by a solid–hexatic–liquid transition [1, 2, 3]. Micron sized colloidal particles with radii  $R_0$  trapped at a fluid interface form a monolayer and constitute an easily accessible mesoscopic model system which exhibits many characteristics of truly 2D systems. This system can actually have fluid and crystalline phases [4], as well as a hexatic phase [5]. Applications may involve controlled self assembly [6] and structure formation [7, 8, 9], exploiting the specific features of the interactions between colloidal particles.

Specifically, the focus of the present study is 2D particle aggregation due to interactions induced by interfacial deformation, i.e., capillary attraction (see, e.g., Refs. [10, 11] and references therein). We consider a collection of colloidal particles at the interface between two fluid phases, each colloid being acted upon vertically by an external force  $f$  (due to, e.g., gravity, an external electric field, an optical tweezer, etc.; see Fig. 1 and Ref. [12]).

In the limit of small interfacial deformations or, alternatively, if the interparticle separation  $d$  between the centers of the colloids is large enough, the effective capil-

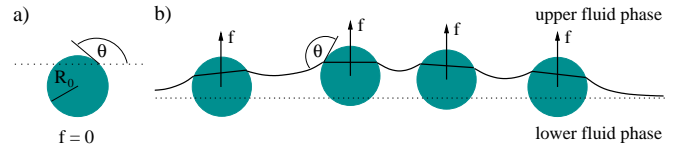


**Fig. 1.** a) A single colloid adsorbed at a fluid interface (dotted line) with no external forces present. b) Identical particles trapped at the interface between two fluids and deforming it due to an external force  $f$  acting on each of them [12] Upwards pointing forces are taken to be positive. In all cases the interface meets the surfaces of the colloids under a fixed contact angle  $\Theta$ .

lary attraction is described by the pair potential [13, 14, 15, 16, 17, 18, 19]

$$V_{\text{cap}}(d) = -V_0 K_0 \left( \frac{d}{\lambda} \right), \quad V_0 := \frac{f^2}{2\pi\gamma}; \quad (1)$$

$\lambda := \sqrt{\gamma/(g\Delta\rho)}$  is the *capillary length*, which determines the range of the interaction and is given in terms of the gravitational acceleration  $g$ , the surface tension  $\gamma$  of the interface, and the mass density difference  $\Delta\rho$  between the two fluid phases. The prefactor  $V_0$  sets the strength of the interaction and  $K_0$  denotes a modified Bessel function. Due to  $V_{\text{cap}}(d \ll \lambda) \sim \ln d$ , in that range the potential is non-integrable (in the sense of equilibrium statistical mechanics, i.e., leading to a hyperextensive scaling of the

energy), while for  $\lambda$  finite  $V_{\text{cap}}(d \gg \lambda) \sim \exp(-d/\lambda)$ . This functional dependence is analogous to screened electrostatics or gravity in 2D, with  $\lambda$  playing the role of the screening length and  $f$  the role of the electric charge or the gravitational mass. The difference with electrostatics is that here equal (different) charges attract (repel) each other, and the difference with gravity is that here one can have negative as well as positive masses. Typically,  $\lambda$  is of the order of a few millimeters so that  $\lambda \gg R_0$ . This implies that a single particle interacts with many neighbors through a non-integrable potential and, in this sense and range, the capillary attraction formally qualifies as a long-ranged interaction. Long-ranged interactions enjoy significant current interest (see, e.g., Ref. [20] and references therein) in many fields, such as self-gravitating fluids in cosmology, two-dimensional vortex flow in hydrodynamics, and bacterial chemotaxis in biology [21, 22]; for the present study the theoretical background reviewed in Ref. [23] is of particular interest.

In Ref. [12] the instability of an initially homogeneous particle distribution, induced by capillary attraction, has been analyzed. The instability is analogous to Jeans' instability of a self-gravitating fluid [24, 25], except for the presence of the screening length  $\lambda$ . Since the parameters  $f$ ,  $\lambda$ ,  $\gamma$ ,  $R_0$  as well as state variables like particle density and temperature are easily tunable, the range of values of the parameters for the observation of this instability for realistic experimental configurations has been explored in Ref. [12]. Even though the capillary attraction between two isolated particles can be relatively weak compared with other effects like thermal agitation and short-ranged repulsive forces, its long-ranged nature (in the sense  $\lambda \gg R_0$ ) leads to a cumulative effect and to an eventual predominance of the capillary force at large scales [26]. Thus, these colloidal monolayers turn out to be excellent model systems for the experimental study of the collective evolution driven by the pair potential given in Eq. (1). We are aware, however, of only one systematic experimental study of this instability with colloidal monolayers [27], in which the long-ranged capillary interactions have been identified as the driving forces of particle aggregation.

Here we perform numerical simulations in order to extend the results reported in Ref. [12] by going beyond the simplifying assumptions underlying the theoretical analysis presented there. The paper is organized as follows. In Sec. 2 we briefly recall the main theoretical results obtained in Ref. [12], followed in Sec. 3 by a description of the algorithm of the simulation used here. This includes in particular a detailed account of how the long-ranged nature of the capillary interaction is handled, similar to the approach for simulations of cosmological structure formation. Section 4 presents the analysis of the simulations, both for the evolution of an unstable homogeneous distribution and the evolution of a radially symmetric particle density. Particular interest is paid to the dependence of the results on the ratio between the capillary length  $\lambda$  and the size  $L$  of the system. This allows one to track the crossover between non-integrability ( $R_0, L \ll \lambda$ ) and

screening ( $R_0 \ll \lambda \ll L$ ). Our conclusions are discussed and summarized in Sec. 5.

## 2 Theoretical model

In this section we briefly describe the theoretical model introduced in Ref. [12], which serves as the basis for the simulations presented here.

Upon projection onto the reference plane, for a contact angle of  $\Theta = 90^\circ$ , the configuration of spherical particles of radius  $R_0$  is mapped onto a configuration of monodisperse discs of radius  $R_0^1$ , the centers of which form an areal number density  $\varrho(\mathbf{r} = (x, y), t)$ , which evolves as a function of time under the action of two types of (effective) forces: the capillary force and a short-ranged repulsive force such as hard core or electrostatic repulsion. Within this model, the dynamical evolution of  $\varrho(\mathbf{r}, t)$  is obtained under the following simplifying assumptions.

- *Local equilibrium*: The characteristic time scales of evolution are sufficiently large so that the forces can be described by a local equilibrium ansatz. For the short-ranged forces the force per unit area is  $(\nabla = (\partial_x, \partial_y))$

$$\mathbf{F}_{\text{short}}(\mathbf{r}, t) \approx -\nabla p(\varrho = \varrho(\mathbf{r}, t)), \quad (2)$$

expressed in terms of the equilibrium equation of state for the pressure  $p(\varrho)$  of the 2D gas of discs in the absence of capillary deformations. Isothermal conditions are assumed. The temperature is a constant parameter fixed by the upper and lower fluids acting as thermal baths, and thus it is irrelevant for the temporal evolution.

- *Mean field*: The capillary force is computed assuming that the interfacial deformation is small and adjusts instantaneously to the momentary particle distribution, i.e., it satisfies the Young-Laplace equation for a given particle distribution  $\varrho(\mathbf{r}, t)$ . Furthermore, a mean-field approximation is used so that the capillary force per unit area can be expressed as

$$\mathbf{F}_{\text{cap}} = f\varrho\nabla U, \quad (3)$$

with the ensemble averaged mean-field interfacial deformation  $U(\mathbf{r})$ . By using  $U(\mathbf{r})$  one neglects spatial variations on small scales, because it is determined self-consistently by the mean-field Young-Laplace equation:

$$\nabla^2 U - \frac{U}{\lambda^2} = -\frac{f}{\gamma}\varrho. \quad (4)$$

Accordingly it is computed from the *average* density field  $\varrho(\mathbf{r}, t)$  rather than from the density field *conditional* to the presence of a particle at  $\mathbf{r}$  [12]. The pair potential in Eq. (1) can be expressed as  $V_{\text{cap}}(d) = fU_\delta(d)$  in terms of Green's function  $U_\delta(d)$  of Eq. (4), i.e., the solution for a single-particle source  $\varrho(\mathbf{r}) = \delta(\mathbf{r})$ . This approximation is justified by the long range  $\sim \lambda$  (see Eq. (1))

<sup>1</sup> The actual deformation of the interface due to external forces  $f$  acting on a colloidal particle is small compared with its radius  $R_0$  [16]. Therefore, for a contact angle of  $\Theta = 90^\circ$ , the discs have approximately the same radius as the spherical colloids.

of the capillary force: if  $\varrho_h$  is a characteristic homogeneous particle number density, the number of particles with which a single particle interacts is effectively of the order  $\varrho_h \lambda^2 \sim (\lambda/R_0)^2 \gg 1$ .

• *Overdamped motion*: Inertia of the particles is neglected, so that the in-plane velocity field  $\mathbf{v}(\mathbf{r}, t)$  of the 2D particle distribution is proportional to the driving force,

$$\varrho \mathbf{v}(\mathbf{r}, t) = \Gamma(\mathbf{F}_{\text{short}} + \mathbf{F}_{\text{cap}}), \quad (5)$$

where  $\Gamma$ , in units of time per mass, is the effective single-particle mobility at the interface. For reasons of simplicity in Eq. (5) the effect of hydrodynamic interactions is neglected and  $\Gamma$  is taken to be constant in space and time<sup>2</sup>.

Under these conditions, mass conservation leads to the following form of the continuity equation:

$$\frac{\partial \varrho}{\partial t} = -\nabla \cdot (\varrho \mathbf{v}) = \Gamma \nabla \cdot (\nabla p - f \varrho \nabla U). \quad (6)$$

Qualitatively, this equation describes the competition between clustering driven by the capillary attraction and the homogenization tendency caused by the short-ranged forces. The solutions of this equation have been studied theoretically in Ref. [12] under certain simplifying conditions. The corresponding findings can be summarized as follows:

• *Jeans' instability*: With the homogeneous density field  $\varrho_h$  one can associate Jeans' time,

$$\mathcal{T} = \frac{\gamma}{\Gamma f^2 \varrho_h}, \quad (7)$$

and Jeans' wavenumber,

$$K = \sqrt{\frac{f^2 \varrho_h^2 \kappa_h}{\gamma}}, \quad (8)$$

where  $\kappa_h = (\varrho_h p'(\varrho_h))^{-1}$  is the isothermal compressibility corresponding to the equation of state  $p(\varrho)$  for a homogeneous configuration. A linear stability analysis shows that a small sinusoidal perturbation  $\varrho_{\mathbf{k}}(\mathbf{r}, 0) = C \varrho_h \exp(-i\mathbf{k} \cdot \mathbf{r})$ ,  $|C| \ll 1$ , of the initially homogeneous distribution  $\varrho_h$  evolves in time as

$$\varrho_{\mathbf{k}}(\mathbf{r}, t) = C \varrho_h \exp(-i\mathbf{k} \cdot \mathbf{r} + t/\tau(k)), \quad (9)$$

with a wavenumber-dependent characteristic time

$$\tau(k) = \mathcal{T} \left( \frac{K}{k} \right)^2 \left[ \frac{1}{(k/K)^2 + (\lambda K)^{-2}} - 1 \right]^{-1}. \quad (10)$$

From this expression one infers that long-wavelength perturbations with

$$k < K_c := K \sqrt{1 - \frac{1}{(\lambda K)^2}} \quad (11)$$

<sup>2</sup> Hydrodynamic interactions play an important role in the process of particle trapping by the interface, as studied recently in Ref. [28]. However, the present theory only considers the evolution *in* the plane of the interface *after* the particles have been trapped there and equilibrium with respect to their distribution normal to the interface has been reached.

grow in time, i.e.,  $\tau(k) > 0$ . Thus the homogeneous state is unstable, provided  $\lambda K > 1$ . This is known as Jeans' instability in a 3D self-gravitating gas [24, 29].

• *Cold collapse*: This approximation amounts to neglecting  $\mathbf{F}_{\text{short}}$  in Eq. (5) relative to the capillary force. (The notion ‘‘cold collapse’’ points to the interpretation of this approximation as the zero temperature limit, in which the classical pressure  $p$  would vanish formally.) This allows one to study the nonlinear stage of a capillary-driven collapse under further simplifying assumptions: considering a radially symmetric particle distribution  $\varrho(r, t)$  and taking  $\lambda \rightarrow \infty$  (which can be phrased as the *Newtonian limit*), one can solve exactly the equation for the radius  $R(t)$  of a ring of particles. For our present purposes, we consider the particular configuration of an initial so-called top-hat density profile,

$$\varrho(r, 0) = \begin{cases} \varrho_h, & r < L, \\ 0, & r > L, \end{cases} \quad (12)$$

with initial size  $L \ll \lambda$  so that the Newtonian limit holds at all times. The trajectory  $R(t)$  of any single ring of matter can be obtained by specializing the general solution given in Ref. [12] to this particular configuration:

$$R(t) = R(0) \sqrt{1 - \frac{t}{\mathcal{T}}}, \quad (13)$$

expressed in terms of Jeans' time as defined in Eq. (7). This result predicts that the whole matter collapses at the center simultaneously at a time  $t = \mathcal{T}$ . The ensuing divergence of this density field is actually preempted by the breakdown of the cold-collapse approximation at sufficiently high densities, because the force  $\mathbf{F}_{\text{short}}$  halts further collapse.

This approximation has also been used in Ref. [12] in order to predict qualitatively the time of collapse of spontaneous fluctuations around a homogeneous background density  $\varrho_h$ : due to the underlying granular nature of the density field, in a surface area  $\mathcal{A} (\ll \lambda^2)$  there are unavoidable fluctuations with an amplitude  $\approx \sqrt{\varrho_h \mathcal{A}}$ . Within the cold-collapse approximation, such initial fluctuations would collapse within the time

$$\mathcal{T}_{\text{coll}} \approx \mathcal{T} \ln \sqrt{\varrho_h \mathcal{A}}. \quad (14)$$

In view of the weak logarithmic dependence, this result predicts that for practical purposes fluctuations at all length scales collapse on a time scale  $\sim \mathcal{T}$ .

In summary, the character of the dynamical evolution is set by two length scales: Jeans' length  $K^{-1}$ , above which the capillary attraction dominates over short-ranged repulsion, and the capillary length  $\lambda$ , above which the capillary attraction vanishes. Finally, the short-ranged repulsive forces set the minimum interparticle separation at which aggregation stops.

### 3 Brownian dynamics simulation

In this section we describe a theoretical approach for colloidal particles floating at an interface which is distinct

from the one given by Eqs. (2)-(6). To this end we consider a two-dimensional collection of  $N$  disc-like particles enclosed in a square box of size  $L \times L$  with periodic boundary conditions. Note that  $L$  always denotes the system size which is either the side length of a square box or the diameter of a rotationally symmetric configuration.

These particles interact via a short-ranged repulsive potential  $V_{\text{rep}}(d)$  which avoids overlap. Specifically, we chose a shifted and cut-off Lennard-Jones potential mimicking the hard core repulsion between the particles:

$$\frac{V_{\text{rep}}(d)}{k_B T} = \begin{cases} 4 \left[ \left( \frac{2R_0}{d} \right)^{12} - \left( \frac{2R_0}{d} \right)^6 + \frac{1}{4} \right], & d \leq d_c \\ 0, & d \geq d_c, \end{cases} \quad (15)$$

where  $R_0$  is the radius of the discs and  $d_c/(2R_0) = 2^{1/6} \approx 1.122$  the cut-off distance. In addition, a given particle is exposed to the capillary force from the other ones (see below). As noted before, we neglect any hydrodynamic interactions, a systematic treatment of which is beyond the scope of the present work.

Due to the coupling to the two fluid phases, the discs experience stochastic forces and their motion is overdamped leading to dissipation. This kind of motion is described by Brownian dynamics. Applying the Ermak algorithm [30] and using the notation introduced in Ref. [31], the integration of the corresponding Langevin equation yields for the change of the position of each disc

$$\dot{\mathbf{r}} = \Gamma \bar{\mathbf{f}} + \dot{\mathbf{r}}, \quad (16)$$

where  $\dot{\mathbf{r}}$  is a random velocity with  $\langle \dot{\mathbf{r}} \rangle = 0$  and  $\langle \dot{\mathbf{r}}_i(t) \dot{\mathbf{r}}_j(t') \rangle = \delta(t-t') \delta_{ij} \mathbb{1}$  [31]. The probability distribution of  $\dot{\mathbf{r}}$  is taken to be uniform with a width  $w$  depending on the time step  $\Delta t$ :

$$w(\Delta t) = \sqrt{2D\Delta t}, \quad D := k_B T \Gamma. \quad (17)$$

It turns out that choosing a Gaussian distribution instead does not change the results of the present study. The flow velocity is  $\mathbf{v} = \langle \dot{\mathbf{r}} \rangle$  and the force per particle is  $\bar{\mathbf{f}} = (\mathbf{F}_{\text{rep}} + \mathbf{F}_{\text{cap}})/\varrho$  (see Eq. (5)).

This particle-based model constitutes an alternative description of the system discussed in the previous section. The random displacements of the colloids in combination with the action of the short-ranged repulsive forces give rise to the macroscopic colloidal pressure  $p$ , as used in Eq. (2), with the corresponding equation of state  $p = p(\varrho)$  which, in principle, could be determined within this model.

Generically, the capillary force  $\mathbf{F}_{\text{cap}}$  on a single particle involves a very large number of neighboring particles due to its long range  $\lambda \gg R_0$ . Furthermore, we are also interested in the case that  $\lambda$  exceeds the side length  $L$  of the system. Therefore, the capillary interactions are calculated using the so-called particle-mesh algorithm (PM), as applied in cosmological simulations which face a similar difficulty (see, e.g., Refs. [32,33,34]). The basic idea is to solve Eq. (4) via Fourier transformation ( $\mathcal{F}[g(\mathbf{r})] \equiv \int d^2r e^{-i\mathbf{r}\cdot\mathbf{k}} g(\mathbf{r}) = \hat{g}(\mathbf{k})$ ) on a mesh

(or grid) which discretizes the plane. Accordingly, Eq. (4) leads to

$$\left( -k^2 - \frac{1}{\lambda^2} \right) \hat{U}(\mathbf{k}) = -\frac{f}{\gamma} \hat{\varrho}(\mathbf{k}) \quad (18a)$$

so that

$$U(\mathbf{r}) = \mathcal{F}^{-1} \left[ -\frac{f}{\gamma} \hat{G}(\mathbf{k}) \hat{\varrho}(\mathbf{k}) \right] \quad (18b)$$

where  $\mathcal{F}$  and  $\mathcal{F}^{-1}$  denote the Fourier transformation and its inverse, respectively.  $\hat{G}(\mathbf{k}) = -1/(k^2 + \lambda^{-2})$  is Green's function for this differential equation. The Fourier transformation can be easily implemented using standard Fast Fourier Transform (FFT) routines. The Fourier-transformed density field  $\hat{\varrho}(\mathbf{k})$  is computed from a given  $\varrho(\mathbf{r})$  by constructing a discretized version of the particle density distribution. Also  $\hat{G}(\mathbf{k})$  is discretized such that it respects the periodic boundary conditions.

In order to discretize the density, we have employed so-called mass assignment schemes using two different versions: the so-called Cloud in Cell (CIC) method, in which each particle is distributed between four neighboring cells, and the so-called Triangular Shaped Cloud (TSC) method using nine neighboring cells. The latter one yields an enhanced smoothening of the particle distribution. Depending on the mesh size of the discretization grid, either of these standard methods may be the more accurate choice. For a grid with a mesh size (somewhat) smaller than the particle size, the distribution to four (CIC) or nine (TSC) neighboring cells corresponds to a smeared patch the size of which is approximately the actual particle size. For the discretized Green's function we use

$$G(k_{\text{lm}}) = \frac{1}{-\sin^2(k_x/2) - \sin^2(k_y/2) - \lambda^{-2}} \quad (19)$$

with

$$k_x = \frac{2\pi l}{L}, \quad k_y = \frac{2\pi m}{L}, \quad l, m \in \mathbb{Z}. \quad (20)$$

The capillary force is obtained from the interfacial deformation field via Eq. (3):

$$\begin{aligned} \frac{\mathbf{F}_{\text{cap}}(\mathbf{r})}{\varrho(\mathbf{r})} &= \nabla[fU(\mathbf{r})] \\ &= \mathcal{F}^{-1} \left[ \frac{f^2}{\gamma} i\mathbf{k} \hat{G}(\mathbf{k}) \hat{\varrho}(\mathbf{k}) \right]. \end{aligned} \quad (21)$$

This yields the discretized capillary force *per particle* at the grid points. In order to obtain the actual force at the particle position, one has to interpolate the discretized force using the inverse of the chosen mass assignment scheme.

This method offers two important advantages. First, it is fast because the number of operations of the PM algorithm scales like  $N_g \log N_g$ , where  $N_g$  is the number of nodes of the grid. Second, this method guarantees an appropriate incorporation of the long-ranged potential, i.e., without introducing any cutoffs together with a high accuracy down to small distances of the order of the grid spacing  $r_c$ . We have chosen  $r_c = R_0$ .



In order to save computation time by reducing the number of integration steps, and, even more important, in order to avoid large displacements  $\Delta\mathbf{r}$  by the random velocity process, the time step is not fixed during the simulation, but it is calculated in each iteration step from the requirement that the maximum displacement due to the force acting on any individual colloid should not exceed  $R_0/4$ . This corresponding maximum time step is then used in order to calculate the width of the distribution for the random displacement according to Eq. (17). We note that this displacement, due to the thermal fluctuations, can be larger than the nominal value of  $R_0/4$ . This cut-off distance appears to be small for simulation boxes with  $L \sim 500R_0$ . This is, however, a compromise which on one hand ensures reasonable computational costs, and on the other hand avoids large values of repelling forces. Such forces emerge if a particle is displaced randomly on top of another particle and encounters the hard core of the repulsive potential. At such small distances, the  $r^{-12}$  term in the potential would generate large forces which in turn would lead to large velocities, yielding the approximation of an overdamped motion and thus the Langevin equation for the position inapplicable.

The structure of the simulation algorithm can be summarized by the following main steps:

1. random placement of particles on a plane without overlap;
2. assignment of particles to a grid by means of a mass assignment scheme, resulting in a number density field defined on the grid;
3. Fourier transformation of this density field by application of standard FFT;
4. computation of the capillary force field on the grid according to Eq. (21);
5. interpolation of this force field to the positions of the particles using the inverse mass assignment scheme;
6. calculation of short-ranged repulsive forces by summation over all particles within one box size (minimal image convention);
7. calculation of the maximum possible time step;
8. integration of the equations of motion by using Ermak's algorithm for Eq. (16) and loop back to step 2.

This algorithm approximates Eq. (6) in terms of individual particle positions which, when assigned to a density grid, represent the approximate evolution of  $\varrho(\mathbf{r}, t)$ .

## 4 Results

In order to probe the predictions of the theoretical model reviewed in Sec. 2, for two types of initial configurations with periodic boundary conditions we have carried out the simulations described above for discs of radius  $R_0$  with a short-ranged repulsion according to Eq. (15):

- a random homogeneous distribution of non-overlapping discs in a square box of size  $L \times L$ ,

- a rotationally invariant configuration forming a disc of radius  $L$  surrounded by vacuum, i.e., embedded in an empty square box of size  $L' > 2L$ .

We have chosen the temperature to be low enough so that these configurations are unstable, i.e.,  $\lambda K > 1$  (see Eq. (11)), and the particles therefore tend to lump together under the driving capillary force. The effects specifically due to the long-ranged nature of this interaction can be studied by comparing simulation data for various values of  $\lambda$ . By changing the screening parameter  $\lambda$  the interparticle attraction can be tuned from being de facto short-ranged ( $\lambda$  of the order of a few colloid diameters, such that the minimum image convention applies) to being long-ranged ( $\lambda \rightarrow \infty$ , for which the attraction is formally analogous to 2D Newtonian gravity). At sufficiently low temperatures  $T$ , the behavior of the system is determined by minimizing its potential energy. Thus, for low  $T$  the final state for any system of size  $L$  is a single cluster with maximum close packing of the particles determined by the interparticle repulsion (e.g., due to the hard core of the discs). This cluster will contain most particles. However, the range of the force determines how and on which time scale this final state is reached.

- $R_0, L \ll \lambda$ ; in this limiting case it is expected that phenomena occur which are similar to the gravitational collapse studied in the astrophysical context. In the so-called Newtonian limit ( $\lambda \rightarrow \infty$ ) the theoretical analysis summarized in Sec. 2 suggests that Jeans' time  $\mathcal{T}$  (see Eq. (7)) sets the corresponding characteristic time scale of evolution.
- $R_0 \lesssim \lambda \ll L$ ; in this limit the behavior of the system is expected to be similar to that of a common fluid and the corresponding mean-field description would be analogous to a van-der-Waals type equation of state. The temporal evolution is expected to follow the scenario of spinodal decomposition because the initial density  $\varrho_h$  lies in the unstable region between the liquid and vapor coexistence densities.

One of the goals of the present simulations is to study the crossover between these two limiting behaviors.

We have performed several simulations based on the set of parameter values shown in Table 1, which all correspond to an experimentally realistic choice of parameters. Unless stated otherwise, all simulations are based on the parameter values quoted in Table 1. We always employ initial conditions with such diluted densities that the equation of state of an ideal gas can be applied in order to obtain a rough estimate of Jeans' length from Eqs. (1) and (8):

$$K^2 \approx \frac{f^2 \varrho_h}{\gamma k_B T} = 2\pi \varrho_h \frac{V_0}{k_B T}. \quad (22)$$

### 4.1 Random homogeneous distribution as initial configuration

First we address the quantitative prediction in Eqs. (9) and (10) concerning the early evolution of the initial fluc-

number of colloids	$N$	2500
colloid radius	$R_0$	$10 \mu\text{m}$
system size	$L$	5 mm
capillary length	$\lambda$	2.7 mm
strength of capillary force	$V_0$	$0.89 k_B T$
particle mobility	$\Gamma$	$10.6 \times 10^{-6} \text{s/kg}$
mean particle separation	$L/N^{1/2}$	$100 \mu\text{m}$
Jeans' length	$1/K$	$43.8 \mu\text{m}$
Jeans' time	$\mathcal{T}$	40780 s

**Table 1.** Default values of the parameters used for all simulations presented here and certain quantities deduced from them. The value of  $\lambda$  corresponds to the capillary length of a pure water–air interface and the value of  $\Gamma$  to the effective mobility of a sphere half immersed in water at room temperature [12].

tuations. In Fig. 2 we show the growth of the amplitudes of various modes of the Fourier-transformed initial density field, normalized by their values at  $t = 0$ . The evolution is expected to follow the exponential dependence given in Eqs. (9) and (10). According to these equations, unstable modes are characterized by the condition  $k < K_c$  (see Eq. (11)) with amplitudes increasing with time. We identify the fastest growing mode as the one with  $k = 0.126 K_c$ . Modes with  $k > K_c$ , the amplitudes of which decrease with time, are stable. Up to  $t \sim 1.5\mathcal{T}$ , the agreement with this theoretical prediction is very good. Thus the linearized stability analysis is reliable up to the characteristic time  $\mathcal{T}$  of the system.

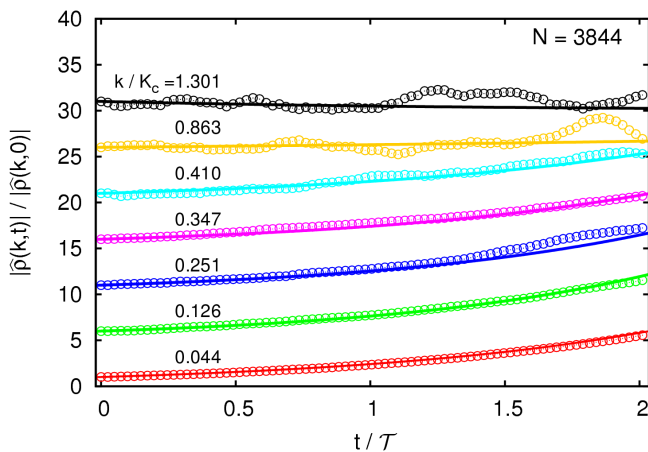


**Fig. 2.** Evolution of Fourier modes  $\hat{\varrho}(|\mathbf{k}| < K_c, t = 0)$  of the initial density distribution (averaged over shells of constant  $k = |\mathbf{k}|$  and each shifted upwards by 5 for clarity) in a simulation for a  $L \times L$  box,  $L = 620R_0$ , with  $N = 3844$  particles. According to Eq. (11) and Table 1,  $K_c = 22.8 \text{mm}^{-1}$  and  $\mathcal{T} = 40780 \text{s}$ . The error bars concerning the statistical errors, as obtained from averaging within small time intervals of the order of  $\Delta t \approx \mathcal{T}/40$  and over 20 runs of initial configurations, are smaller than the symbol size of the simulation data. The full lines provide the corresponding theoretical prediction  $\exp(t/\tau(k))$  as given by Eqs. (9) and (10). The mean initial number density is  $\varrho_h = 10^{-2} R_0^{-2}$ .

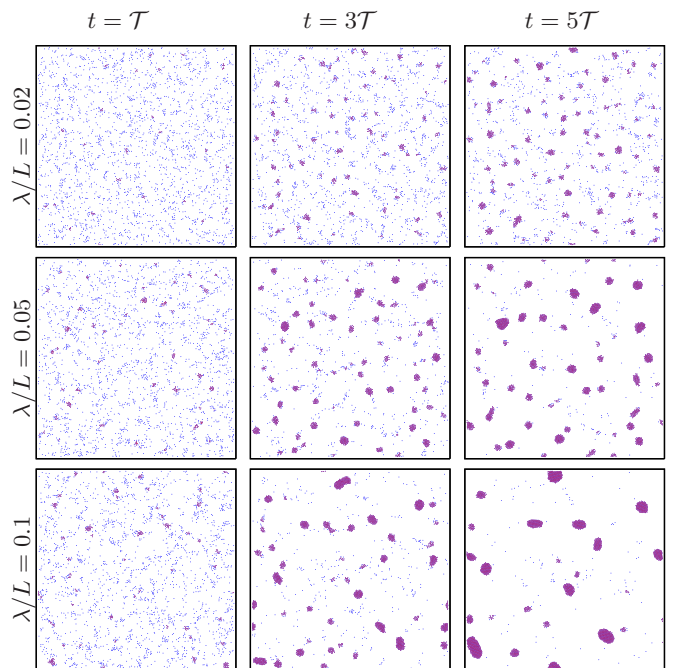


**Fig. 3.** Snapshots of the particle distribution in  $L \times L$  boxes with  $L = 500R_0$  at times  $\mathcal{T}$ ,  $3\mathcal{T}$ , and  $5\mathcal{T}$  for a “short-ranged” capillary attraction with  $\lambda/L = 0.02$ ,  $\lambda/L = 0.05$ , and  $\lambda/L = 0.1$  (from top to bottom). The number of particles is  $N = 2500$ . Particles belonging to a cluster are colored in red.

The simulations allow us to investigate the highly non-linear evolution following the initial clustering stage and thus complement the theoretical analysis presented in Ref. [12]. In Figs. 3 and 4 we show the particle distribution in real space at time steps between  $\mathcal{T}$  and  $5\mathcal{T}$  for several values of  $\lambda$ , while keeping the strength  $V_0$  of the capillary potential fixed (see Eq. (1)). We define a particle to be a member of a cluster (and thus being colored in red) if there are at least three neighboring particles at a distance  $d < 3.25R_0$ . This choice is motivated by the position  $r_{min} \approx 3.25R_0$  of the first minimum in the pair correlation function for a dense packing of discs with the repulsion given by Eq. (15), as deduced from simulations. For  $\lambda \simeq L$  (see Fig. 4) the system exhibits the formation of a few clusters on the time scale set by Jeans' characteristic time  $\mathcal{T}$ . These then merge quickly leaving the system in its final state of a single cluster, which contains basically all colloids. For the longest range of the capillary potential probed by us,  $\lambda/L = 10$ , almost all particles in the system collapse into a single cluster between  $t = 3\mathcal{T}$  and  $t = 4\mathcal{T}$ . These observations provide a qualitative confirmation of the prediction according to Eq. (14) that in the Newtonian limit of the cold-collapse approximation the time scale of evolution is of the order of Jeans' time.

In order to obtain a more quantitative description of these clustering phenomena, the temporal evolution of the total number of clusters  $n_c$  (regardless of their size) is presented in Fig. 5, while Fig. 6 shows the mean cluster

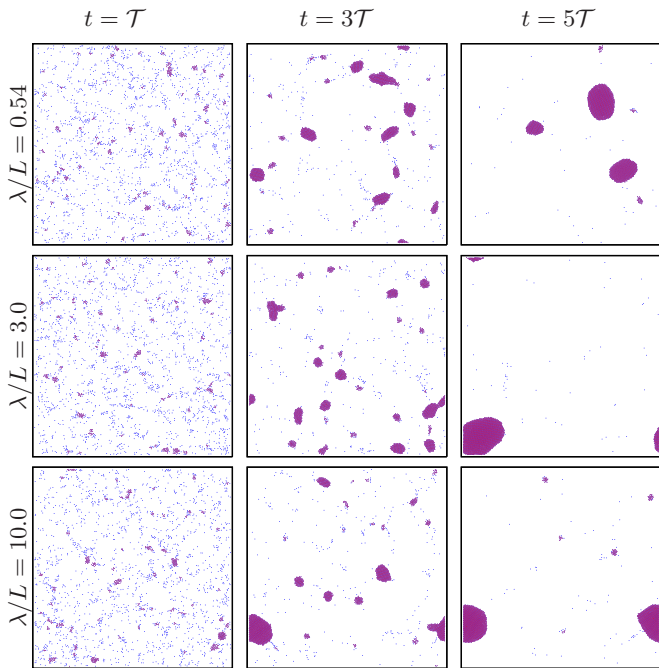


**Fig. 4.** The same presentation as in Fig. 3 for a “long-ranged” capillary attraction with  $\lambda/L = 0.54$ ,  $\lambda/L = 3.0$ , and  $\lambda/L = 10.0$  (from top to bottom).

mass defined as [35]

$$S(t) = \frac{\sum_{s=1}^N s n_c(s, t)}{\sum_{s=1}^N n_c(s, t)}, \quad (23)$$

where  $n_c(s, t)$  is the number of clusters at time  $t$  which consist of  $s$  particles (note that  $n_c(s \leq 3, t) = 0$  according to the definition of clusters introduced before). As  $\lambda$  increases, the evolution of these observables converges to a  $\lambda$ -independent limit characterized by scaling time  $t$  with Jeans’ time. This can be identified with the Newtonian limit ( $\lambda/L \rightarrow \infty$ ) and with the corresponding onset of “long-ranged” dynamics analogous to the gravitational collapse known from astrophysical scenarios. In this limit the temporal evolution extends over a rather short time period ( $\sim 5\mathcal{T}$ ), but nevertheless one can interpret Fig. 5 qualitatively in terms of a two-stage aggregation process: The evolution is initially dominated by the formation of new clusters up to a crossover time  $\sim 1.5\mathcal{T}$ , after which the evolution is dominated by the merging of clusters. This kind of process is not borne out so obviously by Fig. 6 which confirms the steady increase of the average cluster mass, and which seems to follow an exponential law before saturation, induced by finite-size effects, sets in. This latter observation suggests that the average mass  $S(t)$  is biased towards the largest cluster, so that the early evolution of the mass  $s_{\text{large}}(t)$  of the largest cluster can be described by a simple model of accretion of particles (either isolated or in the form of small clusters) at a rate proportional to the capillary attraction by the large cluster, i.e.,

$$\frac{ds_{\text{large}}}{dt} = k s_{\text{large}}, \quad k = \text{const.} \quad (24)$$

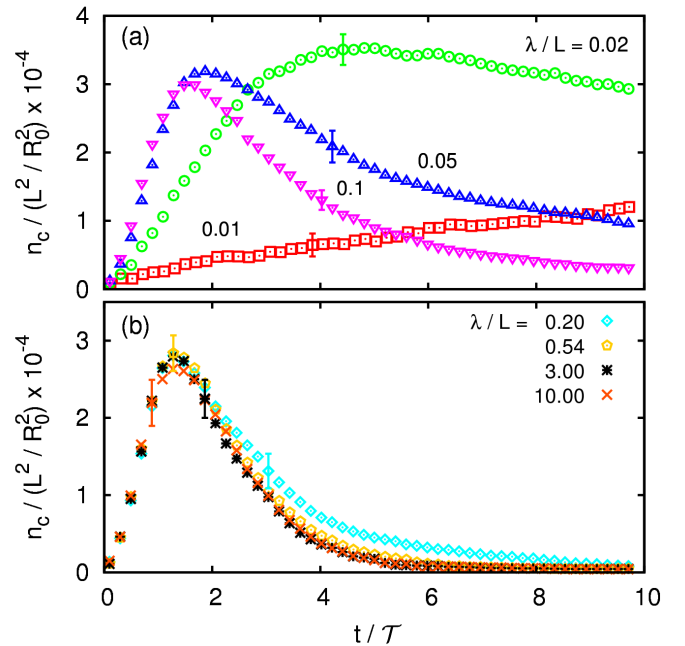


**Fig. 5.** Evolution of the areal number density  $n_c/L^2$  of clusters for several values of  $\lambda/L$ , exhibiting the crossover from “short-ranged” attraction (upper plot (a),  $\lambda \lesssim L$ ) to “long-ranged” attraction (lower plot (b),  $\lambda \gtrsim L$ ). Only representative error bars are shown.

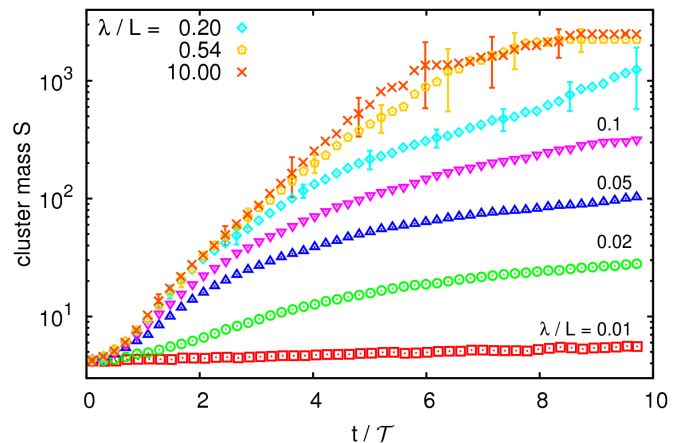


**Fig. 6.** Evolution of the mean cluster mass  $S(t)$  (Eq. (23)) for the same values of  $\lambda$  as in Fig. 5. Only representative error bars are shown. For  $\lambda/L \leq 0.1$  the error bars are of the size of the symbols.

As a complement to these observables, we have also determined the Minkowski functionals (also known as intrinsic volumes, quermassintegrals, or curvature integrals) associated with the density field. Inter alia, these quantities have been applied successfully to the pattern analysis of spinodal decomposition in a 2D van-der-Waals gas [36]. They provide valuable morphological information about the structure formation which is barely accessible by other standard probes such as two-point correlation

functions because the Minkowski functionals are sensitive to higher-order correlations. The properties and applications of these quantities in statistical physics are reviewed in Ref. [37]. Here we provide only the basic corresponding informations required for our present purposes. For a given geometrical domain  $\mathcal{D}$  in the 2D plane, we define the three possible Minkowski functionals  $M_\nu(\mathcal{D})$  as (there are differences in the literature concerning a conventional geometric prefactor)

$$M_0(\mathcal{D}) = \text{area of } \mathcal{D}, \quad (25)$$

$$M_1(\mathcal{D}) = \text{length of the boundary of } \mathcal{D}, \quad (26)$$

$$M_2(\mathcal{D}) = \text{Euler characteristic of } \mathcal{D}. \quad (27)$$

The Euler characteristic  $\chi$  is a measure of the domain connectivity [36,37]:

$$\chi = \text{number of clusters minus number of holes}, \quad (28)$$

where here a “cluster” is defined as a connected subdomain of  $\mathcal{D}$  not connected to other “clusters” (i.e., isolated), and a “hole” is defined as a “cluster” in the complement of  $\mathcal{D}$ , i.e., in the domain  $\mathbb{R}^2 \setminus \mathcal{D}$ . Alternatively,  $\chi$  can be computed also as the integral of the curvature along the boundary of  $\mathcal{D}$  and thus provides a compact measure of whether the boundary of  $\mathcal{D}$  is predominantly convex or concave. For a given density field  $\varrho(\mathbf{r})$  and chosen threshold values  $\varrho_c$ , one can construct domains  $\mathcal{D}(\varrho_c)$  as the regions where the density is larger than the threshold value:

$$\mathcal{D}(\varrho_c) = \{\mathbf{r} \mid \varrho(\mathbf{r}) > \varrho_c\}. \quad (29)$$

The density field  $\varrho(\mathbf{r})$  is computed on a grid with a mass-assignment scheme as described in Sec. 3, except that the grid is coarser than the one used to compute the capillary force (for which the grid spacing is  $r_c = R_0$ , see Table 1). The purpose of this choice is to enhance the smoothening of the density grid; the chosen grid spacing of  $r_{\text{Mink.}} = 5.3R_0$  offers an acceptable compromise between smoothness, accuracy, and computational cost. Accordingly, the density field subjected to such a threshold reduces to a pattern described by pixels and the domain  $\mathcal{D}(\varrho_c)$  is the set of, say, white pixels, for which the Minkowski functionals can be computed efficiently (for details see Ref. [36]).

By construction, the Minkowski functionals are functions of time and of the density threshold  $\varrho_c$ . The latter dependence has been probed in the range between the initial number density  $\varrho_h = (10R_0)^{-2}$  and the density  $\varrho_m = 1/(2\sqrt{3}R_0^2) \approx 29\varrho_h$  of close packing of discs of radius  $R_0$ . The qualitative behavior of the functionals does not depend on  $\varrho_c$  if this value falls within this range (an example for the dependence on the threshold value is presented in Fig. 7). Therefore, in Fig. 8 the time evolution of the three Minkowski functionals is shown only for the threshold value  $\varrho_c = 0.14\varrho_m \approx 4\varrho_h$ . If the threshold value is sufficiently large, as it is the case for  $\varrho_c = 4\varrho_h$ , it is expected that in the domain  $\mathcal{D}$  no “holes” appear, so that  $M_2 > 0$  and gives directly the number of clusters. Furthermore, provided the system is ergodic,  $M_0$  is proportional to the probability distribution of an overdensity,

i.e., that the density at any point is larger than  $\varrho_c$ .  $M_1$  is a direct measure of the length of the “interface” separating clusters (i.e., over-dense regions) from the surrounding low-density gas of particles. The quantities  $M_0/M_2$ ,  $M_1/M_2$  provide an estimate of the average cluster area and perimeter, respectively. We define the “shape factor”  $\phi := M_1^2/(4\pi M_0 M_2)$  which provides a partial, quantitative characterization of the distribution of cluster shapes (see Fig. 9). It is normalized such that  $\phi = 1$  for a single circular cluster.

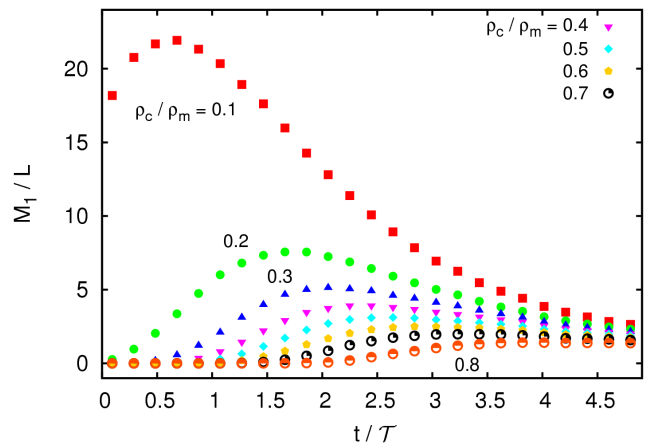


**Fig. 7.** Evolution of  $M_1$  (see Eq. (26)) for various values  $\varrho_c$  of the density threshold within the range  $0.1 \leq \varrho_c/\varrho_m \leq 0.8$ , which corresponds to the range  $3 \leq \varrho_c/\varrho_h \leq 23$ , for  $\lambda/L = 0.54$ ,  $\varrho_m = 29\varrho_h$ , and  $\varrho_h = 10R_0^{-2}$ . Note that for large times,  $M_1/L$  converges to the circumference of a close packed disc ( $M_1/L = \frac{2\pi}{L} \sqrt{N/(\pi\varrho_m)} \approx 0.66$ ; not yet visible on the present scale) for any density threshold. For  $\varrho_c/\varrho_m = 0.1$  the error bars are twice as large as the symbol, in the other cases they are as large as or smaller than the symbol size.

It is interesting to try to understand the simulation results within the framework of spinodal decomposition. In our case, the homogeneous initial distribution (which is the stable equilibrium state if  $\lambda K < 1$ , see Eqs. (8) and (11)) is destabilized by a quench into a coexistence region between a high-density, liquid phase ( $\varrho \sim \varrho_m$ ) and a rather dilute, gaseous phase. Since the average density  $\varrho_h$  is substantially smaller than  $\varrho_m$ , this can be viewed as a quench off the center of the coexistence region with the liquid state being the minority phase. In this context one typically identifies two successive regimes: (i) the early stage of *phase separation* when droplets (i.e., clusters) of the minority phase grow out of the initial fluctuation-induced seeds by binding individual particles, and (ii) the late stage of *domain coarsening* when the droplets coalesce. In Ref. [36], the occurrence of the crossover between these two stages has been identified based on the behavior of the position of the first maximum of the Minkowski functionals as function of time.

Inspection of Figs. 5–9 suggests that this spinodal decomposition scenario is an appropriate interpretation of the present evolution. For  $\lambda/L = 0.01$ , which is the small-



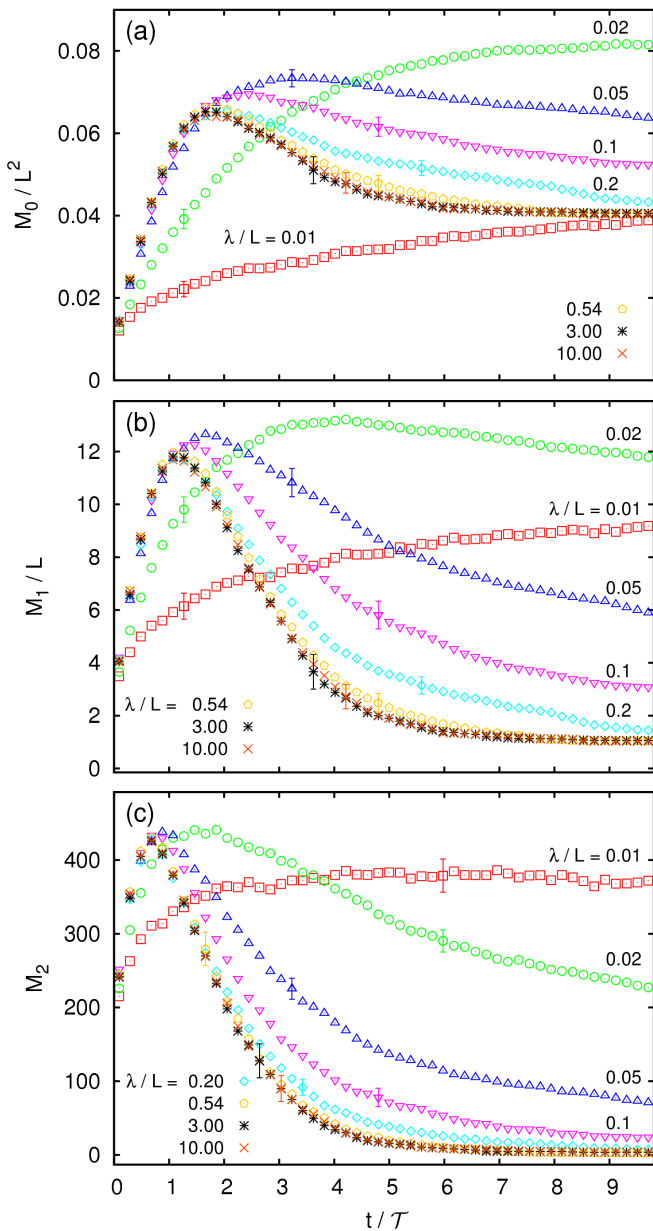


**Fig. 8.** Evolution of the Minkowski functionals  $M_0$  (a),  $M_1$  (b), and  $M_2$  (c) (see Eq. (25)) for the threshold  $\varrho_c = 4\varrho_h = 0.14\varrho_m$  with  $\varrho_h = 10R_0^{-2}$  and for the same values of  $\lambda$  considered in Fig. 5.  $M_0$  is proportional to the area of the region where the density is higher than the threshold value  $\varrho_c$ .  $M_1$  is proportional to the contour length of the boundary of this region whereas  $M_2$  measures the corresponding Euler characteristic. All other parameters of the system are chosen as given in Table 1. Only representative error bars are shown.

est value of  $\lambda$  studied here, one observes only the initial stage of phase separation, marked by a steady increase of  $n_c$  and  $M_2$  (number of clusters),  $S$  (average mass),  $M_1$  (accumulated perimeter), and  $M_0$  (overdensity area). Apparently for this small value of  $\lambda$  the crossover to domain coarsening occurs later than the maximum time of our simulations. However, as evidenced for somewhat larger

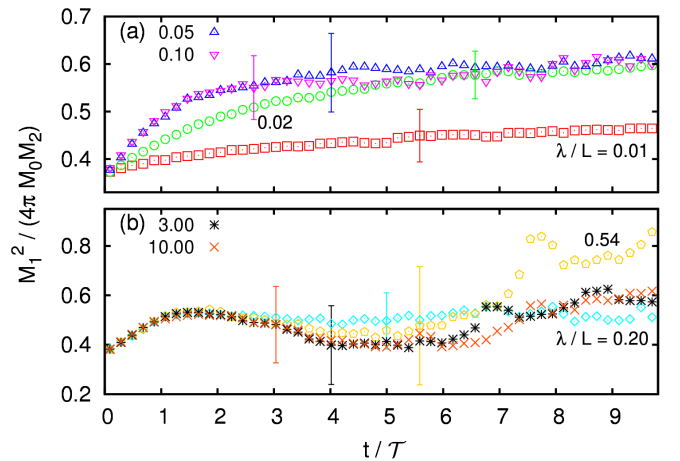


**Fig. 9.** Same as Fig. 8 for the quantity  $\phi = M_1^2 / (4\pi M_0 M_2)$  related to the typical shape of clusters and for the threshold  $\varrho_c = 0.14\varrho_m$ . Note the different scales in panels (a) and (b). Only representative error bars are shown.

values of  $\lambda$ , the shape factor  $\phi$  tends to become time-independent, indicating a self-similar growth of the clusters in the domain-coarsening stage. In the opposite limit, for the largest values of  $\lambda$  explored the crossover to the second stage is clearly observable. It is characterized by the occurrence of maxima followed by a steady decrease of the number of clusters, of the accumulated perimeter, of the overdensity area, and of the shape factor. After the system has collapsed to a single cluster at time  $t \approx 6\mathcal{T}$ , the increase of the shape factor  $\phi$ , although subject to fluctuations, indicates a further compactification and reorganization of the clustered particles towards forming a circular shape. The average mass  $S$ , however, does not exhibit any clear feature indicative of the crossover. It eventually saturates when only a single cluster remains, to which most particles are bound.

We emphasize that this description is valid if the threshold density  $\varrho_c$  takes intermediate values. If  $\varrho_c$  is close to the maximum density  $\varrho_m$ , the signature of the crossover is no longer detectable (see Fig. 7), because in this case the Minkowski functionals just probe the very dense regions, which are formed only at late times and for which the dynamics is presumably no longer dominated by capillary attraction but is instead strongly affected by the short-ranged repulsion.

A characteristic feature of the coarsening stage during spinodal decomposition of a common fluid is a self-similar dynamical scaling. As we have seen, if  $\lambda$  is large the evolution is too fast and the range of times probed by the simulations (a few times  $\mathcal{T}$ ) is too narrow in order to be able to reliably observe a self-similar evolution. However, one can still identify the coarsening stage by means of the extrema in the Minkowski functionals. This demonstrates their robustness even in the extreme case of the almost simultaneous collapse of all length scales, i.e., if most of the wavevectors of the system fulfill  $k < K_c$  (see Eq. (11)) so that the corresponding Fourier components grow rapidly.

This supports the applicability of the Minkowski functionals as advocated in Ref. [36].

In the absence of an elaborated theory, here we can provide only a tentative explanation concerning specifically the influence of  $\lambda$  on the evolution. Our numerical observations can be rationalized assuming that the dependence on  $\lambda$  enters only via the two dimensionless quantities  $\lambda K$  and  $\lambda/L$ . The data suggest that the Newtonian limit ( $1 \ll \lambda/L$ ,  $\lambda K$ ) yields a  $\lambda$ -independent behavior and that the crossover occurs at a time of the order of Jeans' time  $\mathcal{T}$ , in agreement with Eq. (14). For intermediate values of  $\lambda$  ( $\lambda/L \ll 1 \ll \lambda K$ ), only the early-time evolution is  $\lambda$ -independent (in agreement with the analytic linear analysis, see Eq. (10)) whereas the late-time, domain-coarsening stage depends significantly on  $\lambda$ , but the crossover time does so only weakly. Finally, the whole evolution depends sensitively on the value of  $\lambda$  if it is small ( $\lambda/L \ll \lambda K \sim 1$ ): for  $\lambda \gtrsim 1/K$ , the homogeneous state is unstable and undergoes spinodal decomposition, whereas for  $\lambda \lesssim 1/K$  the homogeneous state becomes stable as estimated from mean-field theory (see Sec. 2).

#### 4.2 Radially symmetric initial configuration

In this subsection we test the cold-collapse approximation for radially symmetric configurations. In this context “cold” means that the particles move under the action of the capillary force only, corresponding to the formal limits  $T \rightarrow 0$  (no Brownian motion) and  $R_0 \rightarrow 0$  (no short-ranged repulsion). The first limit is easily attained by switching off the random displacement i.e.,  $\dot{\mathbf{r}} = 0$  in Eq. (16) leading to a deterministic Langevin equation (see Eq. (17)). In order to comply with the second limit we adopt a sufficiently large initial mean interparticle separation, so that the cold-collapse evolution can be followed numerically over some time. This way the breakdown of the cold-collapse approximation can be monitored realistically in those regions where the density approaches its largest possible value. All simulations have been carried out for  $N = 451$  particles arranged as a disc with initial radius  $L = 183R_0$  contained in a quadratic simulation box with side length  $L' = 800R_0$ . Radial symmetry is achieved approximately by surrounding the collapsing disc with a ringlike stripe of vacuum of thickness  $\approx 220R_0$ . For simulations in which the radius of the disc is smaller than  $\lambda$ , the additional stripe of vacuum ensures that the periodic images, which violate the rotational symmetry, contribute only weakly to the total force experienced by the particles. We have run two sets of simulations:

1. In the first set, temperature has been switched off and particles are initially ordered in suitable concentric rings with equal spacing (arc length  $\approx 12.12R_0$ ) along the circumference of all rings, so that each ring possesses discrete azimuthal invariance<sup>3</sup> (see inset of Fig. 10). The azimuthal position of the particles is preserved during evolution. These somewhat artificial con-

2. In the second set the previous conditions are relaxed: temperature is switched on as it has been done in the simulations discussed in the previous subsection, and the initial particle distribution inside the disc is random. With this more realistic study we address the effect nonzero temperature has on the theoretical prediction.

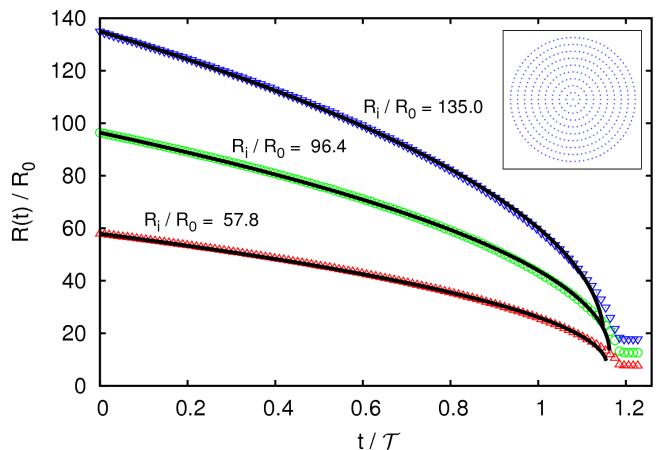


**Fig. 10.** Cold evolution of the radii  $R(t)$  of three rings with initial radius  $R_i/R_0 = R(t=0)/R_0 = 58, 95,$  and  $135$  for the highly ordered initial configuration of concentric rings forming a disc as discussed in the main text (see inset). The full lines correspond to Eq. (30) with  $(A_0, R_f/R_0) = (1.15, 18), (1.16, 13),$  and  $(1.16, 8)$  top down. The quadratic simulation box of size  $L' = 800R_0$  contains initially a disc of radius  $L = 183R_0$ . The number density of particles inside the disc is  $\varrho_h R_0^2 = 4.28 \times 10^{-3}$ . The range of the capillary attraction is  $\lambda/L = 1.48$  and  $\mathcal{T} = 95340$  s.

For the first set of simulations, Fig. 10 shows the evolution of the radial coordinate  $R(t)$  for three rings inside this disc with different initial radii  $R_i$ . Motivated by the theoretical prediction in Eq. (13), which has been obtained in the Newtonian limit within the cold-collapse approximation, the time dependence can be fitted rather well by the following expression:

$$R(t) - R_f = (R_i - R_f) \sqrt{1 - \frac{t}{A_0 \mathcal{T}}}. \quad (30)$$

This expression differs from Eq. (13) in two respects: the ring radius  $R(t)$  is shifted by subtracting the final radius  $R_f$ , and the time scale  $\mathcal{T}$  of collapse is dilated by a factor  $A_0$ . Deviations at later times, such as the smearing out of the square root singularity, can be clearly attributed to the non-vanishing size of the particles and the resulting repulsive forces. The effect of the finite compressibility comes into play in the late stage of the evolution and prevents the vanishing of  $R(t)$ , so that  $R_f \neq 0$ . The factor  $A_0 \approx 1.16$

<sup>3</sup> Each ring is azimuthally invariant with respect to multiples of the angular separation of nearest neighbors in the same ring.

follows from a fit in the range  $0 < t < 0.9\mathcal{T}$ . However, as can be seen in Fig. 10, the time  $A_0\mathcal{T}$  offers a reasonable estimate for the *effective* time of collapse in the simulations  $\mathcal{T}_{\text{coll}} \approx A_0\mathcal{T}$ , defined by the condition  $R(\mathcal{T}_{\text{coll}}) = R_f$ . It turns out that the factor  $A_0$  depends only weakly on  $R_i$  and we conjecture that the delayed effective time of collapse  $\mathcal{T}_{\text{coll}}$ , i.e.,  $A_0 > 1$ , is a consequence of the finite value of  $\lambda$ . Additionally, residual effects of the tidal forces of the periodic images might be non-negligible. Both effects tend to weaken the attractive force of the collapsing cluster and thus increase  $\mathcal{T}_{\text{coll}}$ . In order to support this conjecture, in Fig. 11 we show the evolution of the radius  $R(t)$  of the outermost ring (actually  $R_i/R_0 < L$  due to binning and the applied discretization scheme) for three values of the screening length  $\lambda$ . Upon increasing  $\lambda$  the collapse time decreases, eventually leading to a collapse at  $\mathcal{T}_{\text{coll}} = \mathcal{T}$ , i.e.,  $A_0(\lambda \rightarrow \infty) = 1$  in line with Eq. (13). The delay in the effective time of collapse  $\mathcal{T}_{\text{coll}}$  upon decreasing  $\lambda$  is confirmed in addition by a theoretical calculation of the cold-collapse radial trajectories, which is perturbative in the parameter  $1/\lambda$  (see Eqs. (4) and (5) in Ref. [26]). This effective time must be understood as a fitting parameter (according to Eq. (30)) because the analysis presented in Ref. [26] indicates that for a small but non vanishing value of  $1/\lambda$  the (delayed) collapse does not actually occur at the center but at the outer rim of the disk (forming a shock wave within the cold-collapse approximation).

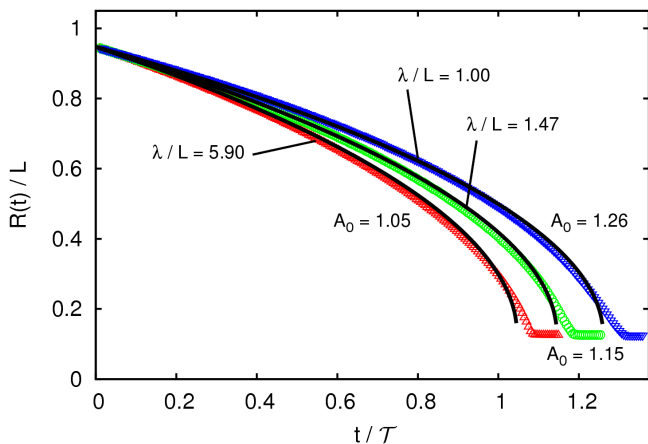


**Fig. 11.** Same as Fig. 10 for the outermost ring ( $R_i/R_0 = 174$ , which is smaller than  $L$  due to binning) for  $\lambda/L = 1, 1.48, 5.9$  and initial disc radius  $L = 183R_0$ . The full lines correspond to the expression in Eq. (30). As expected from Eq. (13) it turns out that  $A_0(\lambda \rightarrow \infty) = 1$ .

For the second set of simulations, Fig. 12 presents the results after averaging over the data sets of ten runs corresponding to different realizations of the random initial configuration. Equation (30) provides a good fit and the conclusions following from it hold also for this kind of data set. The main differences with Fig. 10 are that  $R(t)$  approaches more smoothly its value  $R_f$  of the final, collapsed state, and that this happens at later times: the fit of the

data for the same range  $0 < t < 0.9\mathcal{T}$  shows much larger deviations at later times so that, although for a fixed value of  $\lambda$  an approximately common fitting parameter  $A_0$  can be found,  $A_0\mathcal{T}$  does not provide an equally good estimate for the effective time of collapse  $\mathcal{T}_{\text{coll}}$ . These deviations can be attributed to the Brownian motion and the random initial particle distribution. Both effects tend to spoil the radial symmetry and the sole prevalence of capillary attraction in driving the evolution and slow down the approach to the final state. For the purpose of comparison, the values for Jeans' time and wavenumber associated with the particle density  $\varrho_h = N/(\pi L^2)$  of the discs are  $\mathcal{T} = 95340$  s and  $K = 15.2 \mu\text{m}^{-1}$ , respectively. Since  $K^{-1} \ll L, L'$ , one may have anticipated that the deviations induced by temperature are limited to the smallest length scale, i.e.,  $R_f$ , and relevant only after times of order  $\mathcal{T}$ , as observed indeed.

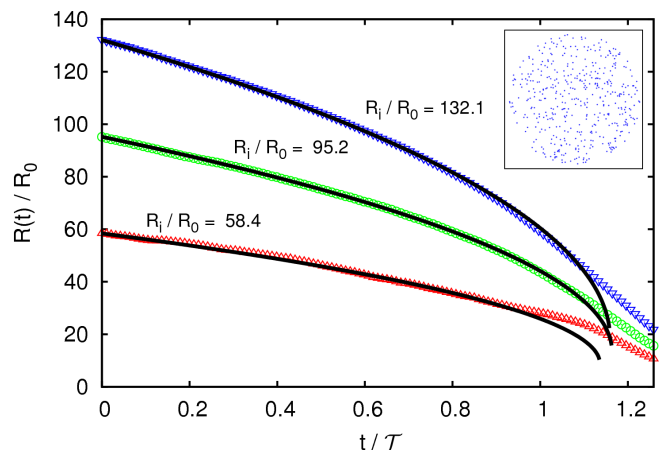


**Fig. 12.** Same as Fig. 10, but for an initial random distribution of particles (see inset) inside a disc of initial radius  $R(0)/R_0 = R_i/R_0$  and with Brownian motion switched on. The radial positions of the particles have been averaged over shells with a bin width of  $\Delta r = 7.5R_0$ . The full lines correspond to Eq. (30) with  $(A_0, R_f/R_0) = (1.16, 18), (1.16, 13), \text{ and } (1.14, 9)$  from top to bottom.

## 5 Summary and conclusions

By means of numerical simulations, we have investigated the clustering of colloidal particles trapped at a fluid interface due to capillary attraction. As explained in detail in Sec. 3, our numerical approach deals with this long-ranged attraction by using a particle-mesh method as employed in simulations of self-gravitating fluids. This is motivated by the formal analogy between capillary and gravitational attraction and because each particle interacts simultaneously with many neighbors. The dynamics is Brownian and describes the overdamped motion of particles in fluids. The key parameters characterizing the macroscopic evolution of initial particle configurations are the range

$\lambda$  of the capillary attraction (Eq. (1)), Jeans' length  $1/K$  (Eq. (8)), and Jeans' time,  $\mathcal{T}$  (Eq. (7)).

A distribution of particles is unstable against clustering provided the capillary attraction is, in a well-characterized sense (see Sec. 2), sufficiently large. Our results confirm the predictions derived theoretically in Ref. [12]: the dynamics evolve linearly during the early stage of evolution up to a time  $\approx 1.5\mathcal{T}$  (see Fig. 2). Also the nonlinear, radially symmetric collapse in the “cold” ( $K \rightarrow \infty$ ) as well as in the “Newtonian” ( $\lambda \rightarrow \infty$ ) limit is well reproduced (see Figs. 10–12). There are small deviations from the theoretical predictions which are due to not reaching this formal double limit.

In addition, the simulations provide insights which go beyond the simplifying approximations underlying the analytic theory. In particular, we have addressed the effect on the instability of the ratio  $\lambda/L$  between the interaction range  $\lambda$  and the system size  $L$ . We have analyzed the nonlinear evolution by using quantitative characteristics which are particularly sensitive to the process of structure formation. These are the number and the mass of clusters as well as the Minkowski functionals of the density field, which have been studied as function of time and of  $\lambda/L$  (see Figs. 5–8). In the “short-ranged limit”  $\lambda \ll L$ , the evolution proceeds on time scales much larger than  $\mathcal{T}$ . During the time probed in our simulations, the evolution is dominated by the steady formation of new clusters out of the seeds in the fluctuating density field. In the opposite, “Newtonian” limit  $\lambda \gg L$ , a  $\lambda$ -independent behavior emerges. The collapse proceeds much faster and is completed at a time  $\approx 5\mathcal{T}$ , thus confirming the conjecture put forward in Ref. [12] that in this limit Jeans' time sets the temporal scale of the evolution. Despite the speed of this evolution, in the clustering process two regimes can be identified: an initial stage dominated by the formation of new clusters up to a time  $\approx 1.5\mathcal{T}$ , and a later stage dominated by cluster merging towards a single, large cluster. This is reminiscent of the spinodal decomposition dynamics in common fluids corresponding to the regimes of phase separation and domain coarsening, respectively.

We interpret this  $\lambda$ -dependence of the dynamics as a crossover in the behavior from that of a 2D common fluid for small  $\lambda$  (slow spinodal decomposition) to that of a self-gravitating fluid for large  $\lambda$  (fast collapse). Our simulation results show to which extent the features of each limiting case is preserved in the other case and they suggest that the dependence on  $\lambda$  is smooth.

Together with the quantitative estimates for  $\mathcal{T}$  and  $K$  provided in Ref. [12], the present results are expected to be helpful for analyzing and interpreting corresponding experimental data. The simulation algorithm can be expanded easily to include the effect of external fields.

J.B. and M.O. thank the German Research Foundation (DFG) for the financial support through the Collaborative Research Center (SFB-TR6) “Colloids in External Fields” Project N01. A.D. acknowledges support by the Spanish Government through grants FIS2008-01339 (partially financed by FEDER funds) and AIB2010DE-00263.

## References

1. J. M. Kosterlitz and D. J. Thouless, *J. Phys. C* **6**, 1181 (1973).
2. P. Bladon and D. Frenkel, *Phys. Rev. Lett.* **74**, 2519 (1995).
3. A. H. Marcus and S. A. Rice, *Phys. Rev. E* **55**, 637 (1997).
4. P. Pieranski, *Phys. Rev. Lett.* **45**, 569 (1980).
5. K. Zahn, R. Lenke, and G. Maret *Phys. Rev. Lett.* **82**, 2721 (1999).
6. N. Bowden, A. Terfort, J. Carbeck, and G. M. Whitesides, *Science* **276**, 233 (1997).
7. J. Aizenberg, P. V. Braun, and P. Wiltzius, *Phys. Rev. Lett.* **84**, 2997 (2000).
8. L. E. Helseth, R. M. Muruganathan, Y. Zhang, and T. M. Fischer, *Langmuir* **21**, 7271 (2005).
9. J. C. Loudet and B. Pouligny, *EPL* **85**, 28003 (2009).
10. M. Oettel and S. Dietrich, *Langmuir* **24**, 1425 (2008).
11. A. Domínguez, in *Structure and Functional Properties of Colloidal Systems*, edited by R. Hidalgo-Alvarez (CRC Press, Boca Raton, 2010), p. 31.
12. A. Domínguez, M. Oettel, and S. Dietrich, *Phys. Rev. E* **82**, 011402 (2010).
13. M. M. Nicolson, *Proc. Cambridge Philos. Soc.* **45**, 288 (1949).
14. D. Y. C. Chan, J. D. Henry Jr., and L. R. White, *J. Colloid Interface Sci.* **79**, 410 (1981).
15. V. N. Paunov, P. A. Kralchevsky, N. D. Denkov, and K. Nagayama, *J. Colloid Interface Sci.* **157**, 100 (1993).
16. M. Oettel, A. Domínguez, and S. Dietrich, *Phys. Rev. E* **71**, 051401 (2005).
17. A. Domínguez, M. Oettel, and S. Dietrich, *J. Phys.: Condens. Matter* **17**, S3387 (2005).
18. M. M. Müller, M. Deserno, and J. Guven, *Europhys. Lett.* **69**, 482 (2005).
19. A. Domínguez, M. Oettel, and S. Dietrich, *J. Chem. Phys.* **128**, 114904 (2008).
20. A. Campa, T. Dauxois, and S. Ruffo, *Phys. Rep.* **480**, 57 (2009).
21. E. Keller and L. A. Segel, *J. Theor. Biol.* **26**, 399 (1970).
22. P.-H. Chavanis and C. Sire, *Physica A* **387**, 4033 (2008).
23. P.-H. Chavanis, *Physica A* **390**, 1546 (2011).
24. J. H. Jeans, *Phil. Trans. Roy. Soc. London A* **199**, 1 (1902).
25. J. Binney and S. Tremaine, *Galactic Dynamics* (Princeton University Press, 2008).
26. J. Bleibel, A. Domínguez, S. Dietrich, and M. Oettel, *Phys. Rev. Lett.*, accepted for publication arXiv:1105.1284 [cond-mat.soft] (2011).
27. A. Vincze, A. Agod, J. Kertész, M. Zrínyi, and Z. Hórvölgyi, *J. Chem. Phys.* **114**, 520 (2001).
28. P. Singh, D. D. Joseph, and N. Aubry, *Soft Matter* **6**, 4310 (2010).
29. M. K. H. Kiessling, *Adv. Appl. Math.* **31**, 132 (2003).
30. D. L. Ermak, *J. Chem. Phys.* **62**, 4189 (1975).
31. M. P. Allen and D. J. Tildesley, *Computer simulation of liquids* (Oxford University Press, 1987).
32. R. W. Hockney and J. W. Eastwood, *Computer Simulation Using Particles* (Hilger, Bristol, 1988).
33. M. Deserno and C. Holm, *J. Chem. Phys.* **108**, 7678 (1998).
34. A. Knebe, “PM Codes” slides available at: <http://popia.ft.uam.es/aknebe/page3/files/ComputationalCosmology/07PMcodes.pdf>.
35. P. Meakin, *Physica Scripta* **46**, 295 (1992).



36. V. Sofonea and K. R. Mecke, *Eur. Phys. J. B* **8**, 99 (1999).
37. K. R. Mecke, in *Statistical Physics and Spatial Statistics*, edited by K. R. Mecke and D. Stoyan, (Springer, Berlin, 2000), p. 111.